

MODELING THE INFRARED EMISSION FROM THE HR 4796A DISK

AIGEN LI AND J. I. LUNINE

Theoretical Astrophysics Program, Departments of Astronomy and Planetary Sciences, University of Arizona, Tucson, AZ 85721;
agli@lpl.arizona.edu, jlunine@lpl.arizona.edu

Received 2003 January 13; accepted 2003 February 19

ABSTRACT

We model the spectral energy distribution (SED) from the mid-infrared to submillimeter of the ringlike disk of HR 4796A, the dustiest A-type star. We consider dust made of either coagulated but otherwise unaltered protostellar interstellar grains or grains that are highly processed in a protostellar/protoplanetary nebula with silicate dust annealed and carbon dust oxidized. Both types of dust are successful in reproducing the observed SED, provided that the grains are highly fluffy, with a vacuum volume fraction of $\sim 90\%$. We find no evidence for the existence of a hot “zodiacal dust” component a few astronomical units from the star, which was suggested by previous workers to account for the $10\ \mu\text{m}$ wavelength emission.

Subject headings: circumstellar matter — dust, extinction — infrared: stars —
planetary systems: protoplanetary disks — stars: individual (HR 4796A)

1. INTRODUCTION

HR 4796A is a nearby (distance to the Earth $d \approx 67 \pm 3$ pc), young, main-sequence (MS) star (age $\approx 8 \pm 3$ Myr) of spectral type A0 V (effective temperature $T_{\text{eff}} \approx 9500$ K). The HR 4796A dust disk has recently aroused considerable interest because (1) it has the largest fractional IR luminosity relative to the total stellar luminosity ($L_{\text{IR}}/L_* \approx 5 \times 10^{-3}$; $L_* \approx 21 L_{\odot}$) among the ~ 1500 A-type MS stars in the Bright Star Catalogue (Jura 1991), (2) unlike the majority of circumstellar disks, the HR 4796A disk displays a ringlike structure peaking at ~ 70 AU from the central star and abruptly truncated both interior and exterior with a width of $\lesssim 17$ AU (Schneider et al. 1999), and (3) its young age places it at a somewhat transitional stage between massive gaseous protostellar disks around young, pre-MS T Tauri and Herbig Ae/Be stars (~ 1 Myr) and much evolved and tenuous debris disks around MS “Vega-type” stars (~ 100 Myr).

The physical and chemical properties of the dust in the HR 4796A disk, which play a significant role in understanding the creation, dynamical evolution, and structural properties of the disk, are poorly constrained:

1. Based on the lifetime of dust against loss by Poynting-Robertson (P-R) drag, Jura et al. (1993) suggested that the HR 4796A dust is larger than $10\ \mu\text{m}$ in radius and that the dust is a remnant of the protostellar nebula.

2. From an analysis of radiation pressure versus gravitational attraction, Jura et al. (1995) found that the minimum radius of grains orbiting HR 4796A is about $3\ \mu\text{m}$ and argued that these grains have undergone measurable coalescence.

3. In order to explain the $\gtrsim 40$ AU inner hole (Jura et al. 1995) and the ≈ 110 K blackbody approximation for the 10 – $100\ \mu\text{m}$ dust emission, Jura et al. (1998) proposed that the HR 4796A grains are largely composed of ice particles with a typical radius of $\sim 100\ \mu\text{m}$ that originate from a protocometary cloud.

4. In order to explain the entire $12.5\ \mu\text{m}$ emission and the $20.8\ \mu\text{m}$ residual emission unaccounted for by their simple model, Koerner et al. (1998) proposed the existence of a tenuous dust component at a distance of 3–6 AU from the star

that is heated to about 200–300 K, similar to the zodiacal dust in our own solar system.

5. From the red reflectance of the disk, Schneider et al. (1999) argued that the mean dust size must be larger than several microns and that the dust is circumstellar debris rather than interstellar in origin.

6. Based on a detailed modeling of the spectral energy distribution (SED) of the HR 4796A disk, Augereau et al. (1999) proposed a two-component model consisting of a cold annulus peaking at 70 AU from the star (made of interstellar dust-type grains ranging from $10\ \mu\text{m}$ to a few meters) and a hot population at 9–10 AU from the star (made of comet-like grains of radii $\approx 450\ \mu\text{m}$).

7. Using the flux ratio at 10.8 and $18.2\ \mu\text{m}$ and assuming “astronomical silicates,” Telesco et al. (2000) inferred a “characteristic” diameter of ≈ 2 – $3\ \mu\text{m}$ and argued that these grains are unlikely to be primordial; instead, they are probably products of recent collisions of large bodies.

It is the purpose of this work to constrain the dust properties (size, composition, and morphology) of the HR 4796A disk. In general, in a dusty system, dust spatial distribution and dust sizes cannot be uniquely determined by the SED alone. Given that the distribution of the dust in the HR 4796A disk is well constrained by the near-IR imaging of scattered starlight (Schneider et al. 1999) and, to a lesser degree, by the mid-IR imaging of dust thermal emission (Jayawardhana et al. 1998; Koerner et al. 1998; Telesco et al. 2000), an attempt is therefore made in this work to infer the HR 4796A dust properties by modeling the full SED from the mid-IR to the submillimeter wavelengths.

Lacking a priori knowledge of the composition of the dust in the HR 4796A disk, we consider two extreme dust types:

1. “Cold-coagulation” dust.—Dust in protoplanetary disks is formed through cold aggregation of unaltered interstellar materials; this is the case in the outer parts of the disk, where interstellar dust originating from the parent molecular cloud (out of which the disk forms) is not likely to have significantly changed its composition during passage through the weak shock front when the disk is first created except that volatile ice mantles around the refractory cores

may partly sublime, but the recondensation of volatiles occurs efficiently behind the shock (see Beckwith, Henning, & Nakagawa 2000 for a review).

2. “*Hot-nebula*” dust.—Dust has undergone significant destruction and modification in protoplanetary accretion disks through annealing of amorphous silicates and oxidation of carbonaceous dust in the warm inner regions of the accretion disk (Gail 2001); turbulent radial mixing (Gail 2001) and/or outflows driven by “*X-winds*” (Shu, Shang, & Lee 1996) then carry this heavily processed dust into cold regions of the disk, where it is mixed with freshly accreted material from the parent molecular cloud. As an extreme, we consider a dust model in which the carbonaceous dust component has been fully destroyed by oxidation so that only crystalline silicate dust remains.

In reality, the dust in protoplanetary disks would undoubtedly be intermediate between heavily processed dust and aggregates of unaltered interstellar dust. Since planetesimals and cometesimals are formed by coagulation of such dust aggregates, the dust generated by collisions of planetesimals and cometesimals should resemble the original dust from which they are built up.

We first discuss in § 2.1 the general constraints on the HR 4796A dust and disk properties. We then model the observed SED in §§ 2.2 and 2.3 in terms of the cold-coagulation model of unaltered interstellar dust and the hot-nebula model with all amorphous silicate dust annealed and all carbonaceous dust oxidized, respectively. We find that, for both models, (1) highly porous grains with a porosity $P \approx 0.90$ provide excellent fits to the entire SED and (2) there appears to be no need for a hot “*zodiacal cloud*” dust component (§ 3.3), which was previously suggested by Koerner et al. (1998) and Augereau et al. (1999). Therefore, the presence of either type of particle in the disk is possible. We show in § 3.2 that, although good fits to the SED can be achieved by models with a single-power-law dust spatial distribution, they are apparently in conflict with the imaging observations of scattered starlight and dust thermal emission. In § 3.5 we calculate the dust IR intensities integrated over the *Space Infrared Telescope Facility* (SIRTF) Infrared Array Camera (IRAC) and Multiband Imaging Photometer (MIPS) bands predicted for our best-fitting models. The major conclusions are summarized in § 4.

2. MODELING THE DUST IR EMISSION

A grain in the optically thin dust disk of HR 4796A absorbs stellar ultraviolet/optical photons and then reradiates the energy in the IR. To calculate the disk’s emission spectrum, knowledge of its morphology, composition, and size is required.

2.1. General Considerations on Dust and Disk Properties

A fluffy structure is expected for dust in protoplanetary disks as a result of its coagulation growth process. We characterize its fluffiness by porosity P , the fractional volume of a vacuum. We assume that all grains are spherical in shape.

In Appendix A we estimate that the cold-coagulation model leads to porous dust consisting of amorphous silicate and carbonaceous materials (and H₂O-dominated ices in regions colder than ~ 110 – 120 K) with a mixing ratio of $m_{\text{carb}}/m_{\text{sil}} \approx 0.7$ [and $m_{\text{ice}}/(m_{\text{sil}} + m_{\text{carb}}) \approx 0.8$ for cold

regions]. For the hot-nebula dust model, we assume that the dust is exclusively composed of crystalline silicate dust (and ices in cold regions).

We assume a power-law dust size distribution $dn(a)/da \propto a^{-\alpha}$, which is characterized by a lower cutoff a_{min} , upper cutoff a_{max} , and power-law index α (where a is the spherical radius). We take $a_{\text{min}} = 1 \mu\text{m}$, the smallest value among previous estimations of a_{min} (see § 1),¹ and $a_{\text{max}} = 1 \text{ cm}$ (this is not a critical parameter since grains larger than $\sim 100 \mu\text{m}$ are like blackbodies, and their IR emission spectra are size-insensitive).

The dust spatial distribution is well constrained by the near-IR imaging of scattered starlight (Schneider et al. 1999) to be a sharply truncated ringlike structure peaking at a radial distance of ~ 70 AU from the star with a characteristic width of $\lesssim 17$ AU. Therefore, we adopt a Gaussian function for the dust spatial density distribution:² $dn(r)/dr \propto \exp\{-4 \ln 2 [(r - r_p)/\Delta]^2\}$, which is characterized by r_p , the radial position where $dn(r)/dr$ peaks, and Δ the FWHM. The dust surface density distribution obtained by integrating dn/dr over the perpendicular (to the disk plane) path lengths can be expressed as $\sigma(r) = \sigma_p \exp\{-4 \ln 2 [(r - r_p)/\Delta]^2\}$, where σ_p is the midplane ($z = 0$) surface density at $r = r_p$. This distribution function, with $r_p = 70$ AU and $\Delta = 12$ AU, was successful in modeling the scattered-light images (Kenyon et al. 1999). A Gaussian-type dust distribution was also adopted by Klahr & Lin (2001) to model the dynamics of the dust ring around HR 4796A. We fix r_p to be at $r_p = 70$ AU and take $\Delta = 15$ AU, the mean value of the determinations of Schneider et al. (1999; $\Delta \lesssim 17$ AU) and Kenyon et al. (1999; $\Delta = 12$ AU). The inner boundary r_{in} is set to be where grains are heated to $\gtrsim 1500$ K, and hence, r_{in} is a function of dust size. For micron-sized grains, the inner boundary is roughly $r_{\text{in}} = 0.15$ AU. The outer boundary is taken to be $r_{\text{out}} = 250$ AU, which is expected from the disk truncation caused by the tidal effects of HR 4796B, a companion star of HR 4796A (Jayawardhana et al. 1998).

Therefore, we are only left with two free parameters: (1) the dust porosity P and (2) the dust size distribution power index α .

Dielectric functions are taken from (1) Draine & Lee (1984) for amorphous silicate dust, (2) Li & Draine (2001a) for crystalline silicate dust, (3) Li & Greenberg (1997) for carbonaceous dust, and (4) Li & Greenberg (1998) for H₂O-dominated ice. The Bruggman effective medium theory (Bohren & Huffman 1983) is used to calculate the mean dielectric functions for the fluffy heterogeneous dust aggregates. Absorption cross sections are obtained using the Mie theory. With the HR 4796A radiation field approximated by the Kurucz model atmosphere spectrum for A0 V stars (Kurucz 1979), dust equilibrium temperatures are then derived by balancing absorption and emission. For a given

¹ A fluffy grain of $a = 1 \mu\text{m}$ with a porosity of $P = 0.90$ consists of ~ 100 constituent individual (interstellar) particles that have a typical size of $a \sim 0.1 \mu\text{m}$ (see Li & Greenberg 1997). Models with a smaller a_{min} ($= 0.1 \mu\text{m}$) and a larger a_{max} ($= 10 \mu\text{m}$) will be discussed in § 3.2.

² Following Kenyon et al. (1999), we assume an exponential, radial-independent, vertical distribution $dn/dr \propto \exp[-(z/\sqrt{2}H)^2]$, where the vertical scale height H is ≈ 0.5 AU. Alternatively, H can be determined from the vertical hydrostatic equilibrium assumption ($H \propto r^{3/2}$; see Appendix B in Li & Lunine 2003). But the knowledge of the dust vertical distribution is not required. The lack of precise knowledge of the dust vertical distribution does not affect our results since in modeling the SED of the HR 4796A disk, what is actually involved is the dust surface density distribution, $\sigma(r)$.

dust size distribution and a given disk structure (dust spatial density distribution), the emergent IR emission spectrum can be obtained by integrating over the dust size range and over the entire disk. The calculated IR spectrum is then compared with the available photometric data for the HR 4796A disk compiled by Augereau et al. (1999).

2.2. Cold-Coagulation Dust Model

We first model the HR 4796A SED in terms of the dust generated from collisions of planetesimals and cometesimals formed in the disk (see § 3.4) through cold coagulation of unaltered interstellar grains from its parent molecular cloud. Using the dust composition discussed in Appendix A, we calculate the model IR spectra for a wide range of dust porosities P and a wide range of dust size distribution power indices α to search for good fits. We note that P refers to the porosity of refractory dust; P will be reduced to P' for dust with ices (see Appendix B).

We illustrate in Figure 1 the best fits obtained for dust with a porosity of $P = 0.95, 0.90, 0.80,$ and 0.60 . Model parameters and results are tabulated in Table 1. It is seen that the best fit is provided by dust with $P \simeq 0.90$ (with a total mass of $\approx 0.67 m_{\oplus}$; model 2)—dust more porous than this is somewhat too hot so that its emission is deficient in the submillimeter wavelength range (see Fig. 1a); on the

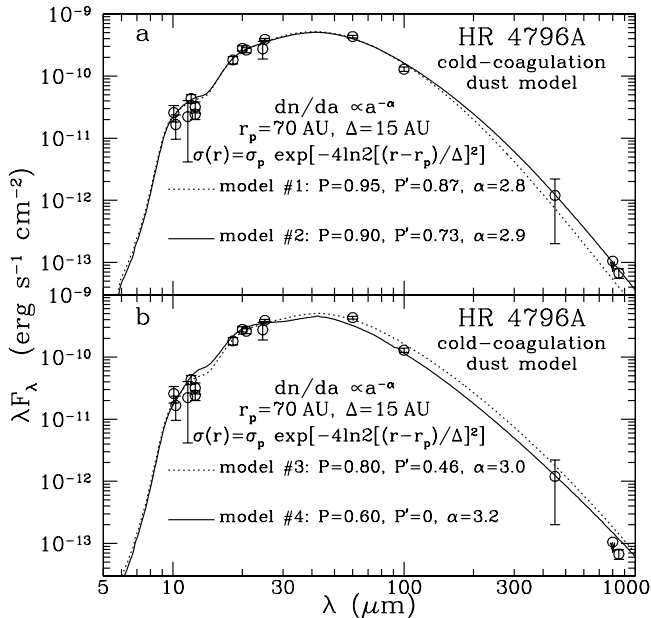


FIG. 1.—Comparison of the observed SED of the HR 4796A dust disk to theoretical IR emission spectra calculated from the cold-coagulation model (porous aggregates of amorphous silicate dust and carbonaceous dust plus ices in cold regions). The dust in this ringlike disk is taken to have a Gaussian distribution function $\sigma(r) = \sigma_p \exp\{-4 \ln^2[(r-r_0)/\Delta]^2\}$ with its peak at $r_p = 70$ AU and an FWHM $\Delta = 15$ AU ($r \in [0.15, 250$ AU]), as inferred from the scattered-light images (Schneider et al. 1999; Kenyon et al. 1999). We assume a power-law dust size distribution $dn(a)/da \propto a^{-\alpha}$ ($a \in [1 \mu\text{m}, 1 \text{cm}]$). (a) The dotted line (model 1) shows the best-fit $P = 0.95$ ($P' \approx 0.87$; see Appendix B) model ($\alpha \approx 2.8$, $m_d \approx 2.67 \times 10^{27}$ g, $\sigma_p \approx 2.97 \times 10^4 \text{ cm}^{-2}$, $\chi^2/N \approx 2.85$, where $N = 18$ [16 data points plus two free parameters P and α ; see text]). The solid line (model 2) shows the best-fit $P = 0.90$ ($P' \approx 0.73$) model ($\alpha \approx 2.9$, $m_d \approx 4.03 \times 10^{27}$ g, $\sigma_p \approx 4.90 \times 10^4 \text{ cm}^{-2}$, $\chi^2/N \approx 1.81$). (b) The dotted line (model 3) shows the best-fit $P = 0.80$ ($P' \approx 0.46$) model ($\alpha \approx 3.0$, $m_d \approx 5.73 \times 10^{27}$ g, $\sigma_p \approx 7.55 \times 10^4 \text{ cm}^{-2}$, $\chi^2/N \approx 6.08$). The solid line (model 4) shows the best-fit $P = 0.60$ ($P' = 0$) model ($\alpha \approx 3.2$, $m_d \approx 4.34 \times 10^{27}$ g, $\sigma_p \approx 1.31 \times 10^5 \text{ cm}^{-2}$, $\chi^2/N \approx 7.60$).

other hand, dust more compact than this is a bit too cold so that it produces too much emission in this wavelength range (see Fig. 1b).

2.3. Hot-Nebula Dust Model

Now we consider another extreme case: dust in the inner disk regions has been so heavily processed that all amorphous silicate dust has been annealed ($T \gtrsim 800$ K) and all carbonaceous dust has been oxidized ($T \gtrsim 1100$ K) by reacting with OH. The annealed silicate dust is then transported to (or the silicate vapor recondenses in crystalline form in) the cold outer regions of the disk, where these grains grow into fluffy aggregates and are ultimately built into planetesimals/cometesimals. Apparently, only a fraction of the dust in the disk is accreted to the inner warm regions, and hence, only a fraction of the silicate dust is crystalline. But since we are considering an “extreme” case, in this section we model the hot-nebula dust as porous aggregates of *pure* crystalline silicate dust (plus ices in cold regions where dust reaches a temperature of $\lesssim 110$ – 120 K). We do not know how much ice would recondense on the silicate core seeds in the fluffy aggregate, but the assumption of full condensation of all condensable volatile elements (C, O, N) as ices (see Appendix A) seems to be at the highest end. As a complement to § 2.2, where full condensation is assumed, we take $v_{\text{ice}}/v_{\text{sil}} = 1$, a plausible value for dense molecular clouds.

Again, model IR spectra are calculated for a wide range of dust porosities P and a wide range of dust power indices α . Except for the sharp features at 11.3 and $23 \mu\text{m}$, the hot-nebula model spectra are very similar to those of the cold-coagulation model. For illustration, we show in Figure 2 the

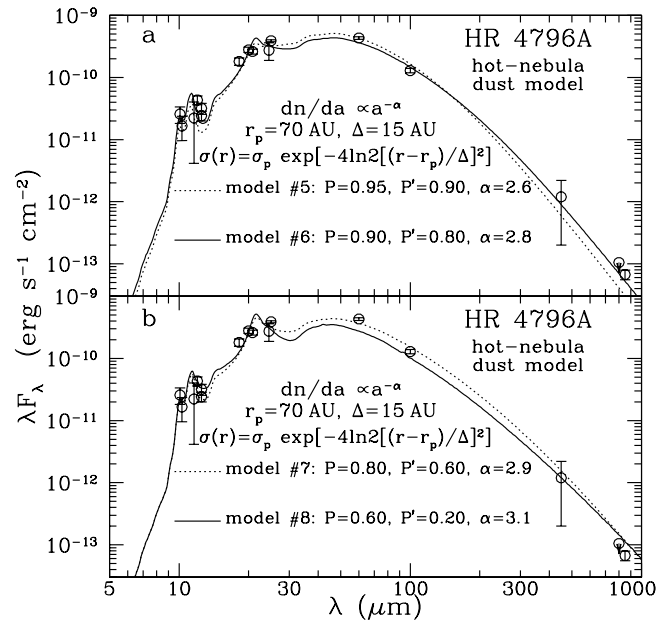


FIG. 2.—Same as Fig. 1, but for the hot-nebula model (porous aggregates of crystalline silicate dust plus ices in cold regions). (a) The dotted line (model 5) shows the best-fit $P = 0.95$ ($P' \approx 0.90$) model ($\alpha \approx 2.6$, $m_d \approx 6.02 \times 10^{27}$ g, $\sigma_p \approx 8.54 \times 10^3 \text{ cm}^{-2}$, $\chi^2/N \approx 5.29$). The solid line (model 6) shows the best-fit $P = 0.90$ ($P' \approx 0.80$) model ($\alpha \approx 2.8$, $m_d \approx 7.48 \times 10^{27}$ g, $\sigma_p \approx 2.55 \times 10^4 \text{ cm}^{-2}$, $\chi^2/N \approx 4.48$). (b) The dotted line (model 7) shows the best-fit $P = 0.80$ ($P' \approx 0.60$) model ($\alpha \approx 2.9$, $m_d \approx 1.16 \times 10^{28}$ g, $\sigma_p \approx 4.30 \times 10^4 \text{ cm}^{-2}$, $\chi^2/N \approx 5.24$). The solid line (model 8) shows the best-fit $P = 0.60$ ($P' \approx 0.20$) model ($\alpha \approx 3.1$, $m_d \approx 9.25 \times 10^{27}$ g, $\sigma_p \approx 8.04 \times 10^4 \text{ cm}^{-2}$, $\chi^2/N \approx 9.94$).

TABLE 1
MODELS FOR THE HR 4796 A DUST DISK IR EMISSION

Model	Dust Type ^a	Spatial Distribution ^b	P	P'	Δ (AU)	β	α	$\langle a \rangle^c$ (μm)	$\langle a^2 \rangle^c$ (μm^2)	$\langle a^3 \rangle^c$ ($\times 10^{-8} \text{ cm}^3$)	m_d ($\times 10^{27} \text{ g}$)	σ_p ($\times 10^4 \text{ cm}^{-2}$)	$\tau_p^{f,d}$	χ^2/N	Notes
1.....	CG	Gaussian	0.95	0.87	15	...	2.8	2.25	47.8	9.46	2.67	2.97	0.041	2.85	
2.....	CG	Gaussian	0.90	0.73	15	...	2.9	2.11	28.7	4.34	4.03	4.90	0.042	1.81	Preferred
3.....	CG	Gaussian	0.80	0.46	15	...	3.0	2.00	18.4	2.00	5.73	7.55	0.043	6.08	
4.....	CG	Gaussian	0.60	0	15	...	3.2	1.83	9.26	0.44	4.34	13.1	0.038	7.60	
5.....	HN	Gaussian	0.95	0.90	15	...	2.6	2.66	155	45.5	6.02	0.85	0.040	5.29	
6.....	HN	Gaussian	0.90	0.80	15	...	2.8	2.25	47.8	9.46	7.48	2.55	0.036	4.48	Preferred
7.....	HN	Gaussian	0.80	0.60	15	...	2.9	2.11	28.7	4.34	11.6	4.30	0.037	5.24	
8.....	HN	Gaussian	0.60	0.20	15	...	3.1	1.91	12.6	0.93	9.25	8.04	0.031	9.94	
9.....	CG	Power-law	0.90	0.73	-2.3	1.83	9.26	0.44	8.43	0.42	0.0011	2.32	
10.....	CG	Power-law	0.90	0.73	-2.5	2.00	18.4	2.00	5.81	0.98	0.0054	3.28	$r \in [40, 130 \text{ AU}]$
11.....	HN	Power-law	0.90	0.80	-1.1	2.9	28.7	4.34	25.5	0.26	0.0022	9.71	
12.....	HN	Power-law	0.90	0.80	5.2	2.6	155	45.5	6.29	0.056	0.0026	2.02	$r \in [40, 130 \text{ AU}]$
13.....	CG	Telesco	0.90	0.73	21	...	2.9	2.11	28.7	4.34	5.41	2.34	0.020	3.60	
14.....	HN	Telesco	0.90	0.80	21	...	2.8	2.25	47.8	9.46	10.0	1.22	0.017	4.89	
15.....	CG	Gaussian	0.90	0.73	15	...	2.8	0.22	0.81	0.15	5.49	193	0.045	3.44	$a_{\text{min}} = 0.1 \mu\text{m}$
16.....	CG	Gaussian	0.90	0.73	15	...	3.1	19.1	1048	117	2.98	0.13	0.042	5.88	$a_{\text{min}} = 10 \mu\text{m}$

NOTE.—Unless otherwise stated, all models assume $a_{\text{min}} = 1 \mu\text{m}$, $a_{\text{max}} = 1 \text{ cm}$, $r_p = 70 \text{ AU}$, and $r \in [0.15, 250 \text{ AU}]$.

^a CG=cold-coagulation; HN=hot-nebula.

^b Dust spatial distribution. “Gaussian”: $\sigma(r) = \sigma_p \exp\{-4 \ln 2[(r - r_p)/\Delta]^2\}$. “Power-law”: $\sigma(r) = \sigma_p \exp\{-0.01(r/\text{AU}) + 1.32\}$ for $r \in [70, 105 \text{ AU}]$, and $\sigma(r) = \sigma_p[-0.01(r/\text{AU}) + 1.32]$ for $r \in [105, 130 \text{ AU}]$. “Telesco”: $\sigma(r) = \sigma_p \exp[-(\Delta/\text{AU}) \ln^2(r/r_p)]$ for $r \in [0.15, 70 \text{ AU}]$.

^c $\langle a^i \rangle = \int_{a_{\text{min}}}^{a_{\text{max}}} da a^i [dn(a)/da] / \int_{a_{\text{min}}}^{a_{\text{max}}} da [dn(a)/da]$. The dust surface mass density can be written as $\sigma(r; m) = \langle m \rangle \sigma(r)$ with the mean dust mass $\langle m \rangle = (4\pi/3)\langle a^3 \rangle \langle \rho \rangle$, where $\langle \rho \rangle \approx 2.5(1 - P) \text{ g cm}^{-3}$ and $\langle \rho' \rangle \approx 1.7(1 - P')$ for the cold-coagulation model, and $\langle \rho \rangle \approx 3.5(1 - P) \text{ g cm}^{-3}$ and $\langle \rho' \rangle \approx 2.4(1 - P')$ for the hot-nebula model (see Appendix B).

^d Vertical optical depth at $\lambda = 0.55 \mu\text{m}$ and $r = r_p$. The reason why τ_p^f is much smaller for models 9–11 is that the bulk of the dust is piled at the edge of the disk, which is unphysical (see § 3.2).

best-fit model spectra provided by dust with $P = 0.95, 0.90, 0.80,$ and 0.60 . Model parameters and results are also tabulated in Table 1. Similar to the cold-coagulation model, the best fit is given by dust with $P \simeq 0.90$ (with a total mass of $\approx 1.25m_{\oplus}$; model 6).

3. DISCUSSION

It is seen in § 2 that, using a simple power-law dust size distribution ($dn/da \propto a^{-\alpha}$, with $\alpha \approx 2.8\text{--}2.9$ and $\langle a \rangle \approx 2 \mu\text{m}$) and a Gaussian-type dust spatial distribution with a peak at $r_p = 70$ AU and an FWHM $\Delta = 15$ AU as inferred from the near-IR imaging observation of scattered starlight (Schneider et al. 1999; Kenyon et al. 1999), both the cold-coagulation dust model (model 2) and the hot-nebula dust model (model 6) are successful in reproducing the observed SED, provided that the dust in the HR 4796A disk is very fluffy, with a porosity $P \approx 0.90$. We note that, since we use this dust spatial distribution, it is expected that our models are also able to reproduce the imaging observations. It is also interesting to note that, as early as 1965, based on a Monte Carlo simulation, Cameron & Schneck (1965) showed that a very open structure with a porosity in the range $0.83 \lesssim P \lesssim 0.89$ is expected for dust aggregates assembled from randomly incident particles.

Both the cold-coagulation model and the hot-nebula model predict a vertical optical depth at visible wavelengths of $\tau^V \approx 0.04$ at $r = r_p$ (see Table 1). This justifies the optically thin treatment employed in the entire paper. This is because in these models, with a power-law index for the size distribution of $\alpha \in [2.6, 3.2]$ (see Table 1), most of the mass of the particles is in the largest grains. However, the opacity per gram of dust ($\kappa_{\text{abs}} \equiv 3Q_{\text{abs}}/[4a\rho]$ where Q_{abs} is the absorption efficiency for these macroscopic grains— $Q_{\text{abs}} \approx 1$ at visible wavelengths) is much smaller than that of micron-sized dust: $\kappa_{\text{abs}} \propto 1/a$. We note that although the maximum dust size a_{max} is not well constrained, the predicted IR emission spectrum and the optical depth are not very sensitive to the precise value of a_{max} since grains larger than $\sim 100 \mu\text{m}$ have $Q_{\text{abs}} \approx 1$ and emit like blackbodies.

3.1. Robustness

The extent to which dust in protostellar disks has been processed prior to incorporation into planetesimals and comets is not known. But it seems plausible that a fraction of precometary materials has been processed in protostellar nebulae, based on the observational presence of crystalline silicate dust in comets (see Wooden 2002 for a summary of the evidence). While at most $\sim 5\%$ of the silicate material is crystalline in the interstellar medium (Li & Draine 2001a), in some comets the fraction of crystalline silicate dust is as high as $\sim 30\%$. Accretion heating in protoplanetary disks is a probable source for the formation site of the crystalline silicate—although ^{26}Al heating of comets and the consequent release of heat in the amorphous-to-crystalline ice transition cannot be ruled out. The warm inner zone of the accretion disk is particularly appealing as a site for the annealing of amorphous silicate. As a result of diffusional mixing induced by turbulence in the optically thick disk (Gail 2001) or outflows driven by reconnecting magnetic field lines (the X-winds model of Shu et al. 1996), a fraction of the annealed silicate dust arrives at the cooler outer part of the disk to be incorporated in icy “cometary” bodies.

Therefore, we expect that the dust generated by collisions among cometary bodies (see § 3.4), for either origin of the crystalline silicate material, should be intermediate between the cold-coagulation dust and the hot-nebula dust. The mixing ratio of these two dust types is unclear. In principle, the $10 \mu\text{m}$ silicate emission feature should allow us to infer the thermal history of silicate dust through the absence or presence (and the mass fraction) of crystalline silicate dust. However, the only available $8\text{--}13 \mu\text{m}$ spectrum shows very weak thermal emission in the silicate feature; its quality is inadequate to discern the detailed spectral features expected from crystalline silicate dust (Sitko, Lynch, & Russell 2000). But in any case, because of the fact that the two extreme models are able to provide close fits to the observed SED, any linear combinations of these two dust types (i.e., any degree of processing/modification) are expected to be able to reproduce the observed SED as well. Therefore, our models are robust.

3.2. Uniqueness

In modeling the SED, dust sizes and dust spatial distribution are coupled. Since the dust spatial distribution we adopted for the HR 4796A disk is well constrained by near-IR images of scattered light (Schneider et al. 1999), the dust properties are more or less uniquely determined: the dust must be very fluffy (with $P \simeq 0.9$); the dust power-law size distribution has an index $\alpha \approx 2.8\text{--}2.9$ and a mean dust size of $\sim 2 \mu\text{m}$ (see Table 1); and the dust composition should be somewhere between the cold-coagulation dust and the hot-nebula dust, although its detailed composition (e.g., the crystallinity of the silicate dust) is yet unknown (see § 3.1).

The dust spatial distribution in the HR 4796A disk was often modeled as a single power law (Jayawardhana et al. 1998; Koerner et al. 1998; Wyatt et al. 1999) or two power-law components (Augereau et al. 1999). For the purpose of comparison, we have also modeled the HR 4796A SED assuming a single-power-law dust distribution $dn/dr \propto r^{-\beta}$ in terms of the $P = 0.90$ ($P' \approx 0.73$) cold-coagulation dust model and the $P = 0.90$ ($P' \approx 0.80$) hot-nebula dust model.³ We consider two disk extents: (1) $r_{\text{in}} = 0.15$ AU $\lesssim r \lesssim r_{\text{out}} = 250$ AU (see § 2.1) and (2) $r_{\text{in}} = 40$ AU $\lesssim r \lesssim r_{\text{out}} = 130$ AU. The latter takes into account the existence of an inner hole with a radius of $\sim 40\text{--}60$ AU, which was first noticed by Jura et al. (1995) from an analysis of *IRAS* and ground-based photometry. The inner hole was later confirmed by mid-IR imaging of dust thermal emission carried out by three independent groups (Jayawardhana et al. 1998; Koerner et al. 1998; Telesco et al. 2000). These mid-IR imaging observations also implied an outer radius of $\sim 110\text{--}130$ AU for the HR 4796A disk. As can be seen in Figure 3, models with a single-power-law dust spatial distribution are also successful in reproducing the observed SED. However, except for the 40 AU $\lesssim r \lesssim 130$ AU hot-nebula model (model 12), all models (models 9–11) require an increasing accumulation of dust toward the outer edge (i.e., $\beta < 0$). This is neither physical nor consistent with the imaging observations of scattered light (Schneider et al. 1999) and dust thermal emission (Jayawardhana et al. 1998; Koerner et al. 1998; Telesco et al. 2000).

³ As in § 2.1, the dust surface density distribution is written as $\sigma(r) = \sigma_p(r/r_p)^{-\beta}$.

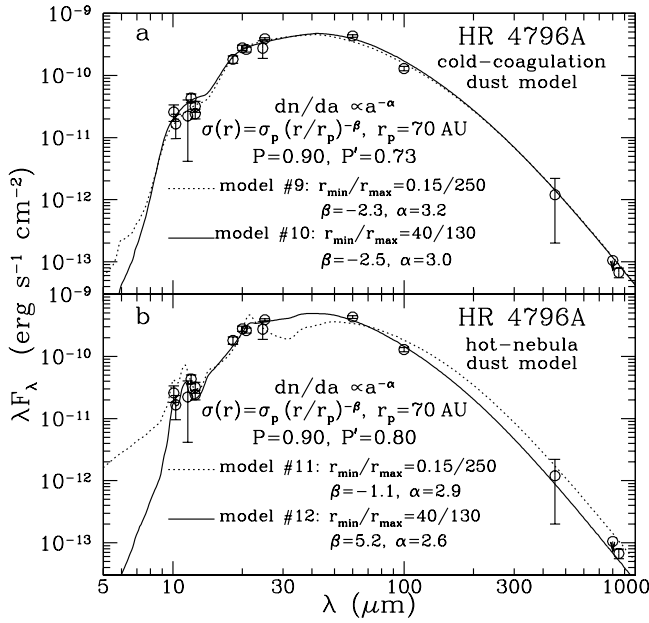


FIG. 3.—Comparison of the HR 4796A observational SED to theoretical IR emission spectra calculated from (a) the cold-coagulation model and (b) the hot-nebula model. The dust spatial distribution is assumed to be a power law $\sigma(r) = \sigma_p (r/r_p)^{-\beta}$ for either $0.15 \text{ AU} \leq r \leq 250 \text{ AU}$ (dotted lines) or $40 \text{ AU} \leq r \leq 130 \text{ AU}$ (solid lines). We assume a power-law dust size distribution $dn(a)/da \propto a^{-\alpha}$ ($a \in [1 \mu\text{m}, 1 \text{ cm}]$). (a) The dotted line (model 9) shows the best-fit $P = 0.90$ ($P' \approx 0.73$) cold-coagulation dust model for $r \in [0.15, 250 \text{ AU}]$ ($\beta \approx -2.3$, $\alpha \approx 3.2$, $m_d \approx 8.43 \times 10^{27} \text{ g}$, $\sigma_p \approx 4.17 \times 10^3 \text{ cm}^{-2}$, $\chi^2/N \approx 2.32$). The solid line (model 10) shows the best-fit $P = 0.90$ ($P' \approx 0.73$) cold-coagulation dust model for $r \in [40, 130 \text{ AU}]$ ($\beta \approx -2.5$, $\alpha \approx 3.0$, $m_d \approx 5.81 \times 10^{27} \text{ g}$, $\sigma_p \approx 9.75 \times 10^3 \text{ cm}^{-2}$, $\chi^2/N \approx 3.28$). (b) The dotted line (model 11) shows the best-fit $P = 0.90$ ($P' \approx 0.80$) hot-nebula dust model for $r \in [0.15, 250 \text{ AU}]$ ($\beta \approx -1.1$, $\alpha \approx 2.9$, $m_d \approx 2.55 \times 10^{28} \text{ g}$, $\sigma_p \approx 2.58 \times 10^3 \text{ cm}^{-2}$, $\chi^2/N \approx 9.71$). The solid line (model 12) shows the best-fit $P = 0.90$ ($P' \approx 0.80$) hot-nebula dust model for $r \in [40, 130 \text{ AU}]$ ($\beta \approx 5.2$, $\alpha \approx 2.6$, $m_d \approx 6.29 \times 10^{27} \text{ g}$, $\sigma_p \approx 5.55 \times 10^2 \text{ cm}^{-2}$, $\chi^2/N \approx 2.02$).

It is expected that models with two-power-law dust spatial distributions are also able to reproduce the observed SED. But the constraints placed by the near-IR and mid-IR imaging observations would imply that the two-segment power-law distribution should not deviate much from the Gaussian function.

Assuming spherical silicate dust of a diameter of $2.5 \mu\text{m}$ (estimated from the 10.8 and $18.2 \mu\text{m}$ emission), Telesco et al. (2000) derived the dust spatial distribution from the $18.2 \mu\text{m}$ brightness distribution (see their Fig. 5). We approximate their result for $r < r_p = 70 \text{ AU}$ as $\sigma \approx \sigma_p \exp[-(\Delta/\text{AU}) \ln^2(r/r_p)]$ ($\Delta \approx 21 \text{ AU}$); for $70 \text{ AU} < r < 105 \text{ AU}$ as $\sigma \approx \sigma_p / \{1 + [(r - r_p)/\Delta]^2\}$; and for $105 \text{ AU} < r < 130 \text{ AU}$ as $\sigma \approx \sigma_p [-0.01(r/\text{AU}) + 1.32]$. In Figure 4 we show that the best-fitting cold-coagulation (model 13) and hot-nebula models (model 14) with this dust distribution also provide close fits to the observed SED.

The overall shape of the Telesco et al. (2000) distribution resembles that of the Gaussian distribution, except that the former is relatively broader and has a flatter wing at $r > 70 \text{ AU}$. Since the Gaussian distribution was derived from scattered-light images that reflect dust of all sizes while the Telesco et al. (2000) distribution was derived only from the 10.8 and $18.2 \mu\text{m}$ mid-IR-emitting dust, we prefer the Gaussian distribution, although the real dust distribution may not be an exact Gaussian function.

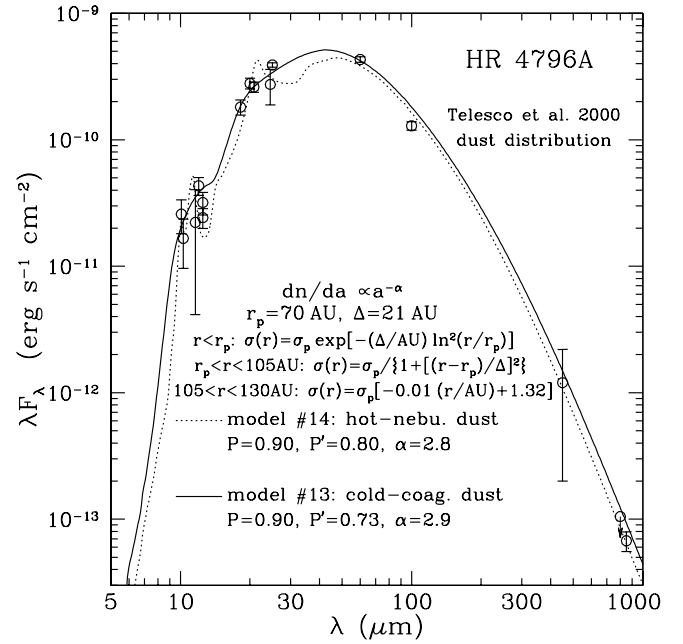


FIG. 4.—Comparison of the HR 4796A observational SED to theoretical IR emission spectra calculated from the cold-coagulation model (model 14 [solid line]; $P = 0.90$, $P' \approx 0.73$, $\alpha \approx 2.9$, $m_d \approx 5.41 \times 10^{27} \text{ g}$, $\sigma_p \approx 2.34 \times 10^4 \text{ cm}^{-2}$, $\chi^2/N \approx 3.60$) and the hot-nebula model (model 13 [dotted line]; $P = 0.90$, $P' \approx 0.80$, $\alpha \approx 2.8$, $m_d \approx 1.00 \times 10^{28} \text{ g}$, $\sigma_p \approx 1.22 \times 10^4 \text{ cm}^{-2}$, $\chi^2/N \approx 4.89$). The dust spatial distribution is taken to be that of Telesco et al. (2000).

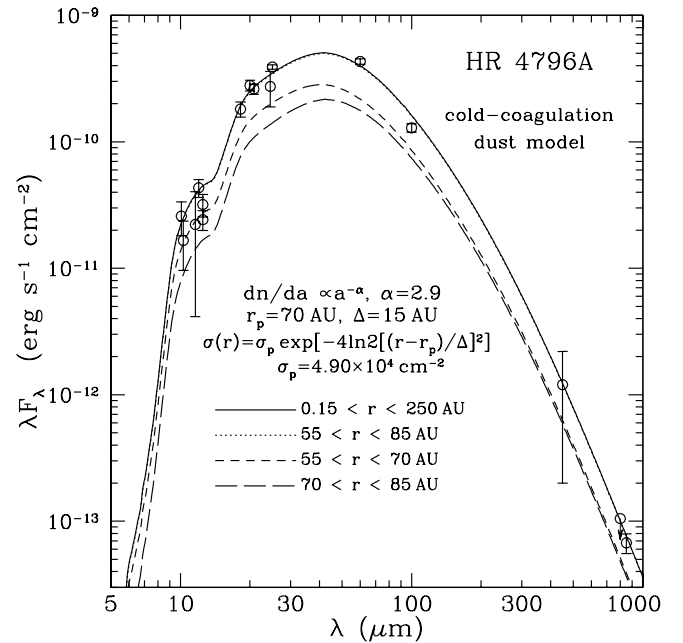


FIG. 5.—IR emission from dust in the ring regions of $r_{\text{in}} = 0.15 \text{ AU} < r < r_{\text{out}} = 250 \text{ AU}$ (solid line; same as the solid line in Fig. 1a), $(r_p - \Delta) < r < (r_p + \Delta)$ (dotted line), $(r_p - \Delta) < r < r_p$ (dashed line), and $r_p < r < (r_p + \Delta)$ (long-dashed line) calculated from the best-fitting cold-coagulation dust model (model 2; $P = 0.90$, $P' \approx 0.73$, $\alpha \approx 2.9$) with a Gaussian spatial distribution ($r_p = 70 \text{ AU}$, $\Delta = 15 \text{ AU}$). The $(r_p - \Delta) < r < (r_p + \Delta)$ spectrum (dotted line) is indistinguishable from the $0.15 \text{ AU} < r < 250 \text{ AU}$ spectrum (solid line).

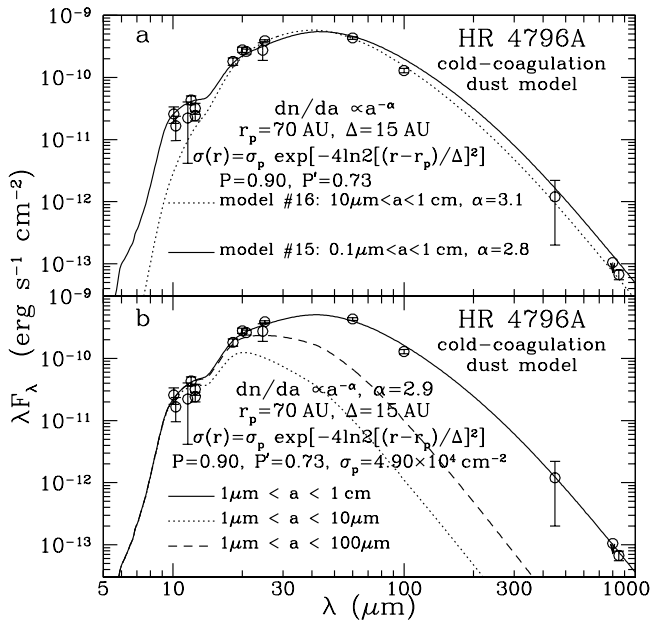


FIG. 6.—(a) Models with smaller a_{\min} ($=0.1 \mu\text{m}$; model 15 [solid line]: $\alpha \approx 2.8$, $m_d \approx 5.49 \times 10^{27}$ g, $\sigma_p \approx 1.93 \times 10^6$ cm⁻², $\chi^2/N \approx 3.44$) and larger a_{\min} ($10 \mu\text{m}$; model 16 [dotted line]: $\alpha \approx 3.1$, $m_d \approx 2.98 \times 10^{27}$ g, $\sigma_p \approx 1.35 \times 10^3$ cm⁻², $\chi^2/N \approx 5.88$). Other model parameters are the same as those of the best-fit cold-coagulation model (model 2; $P = 0.90$, $P' \approx 0.73$). (b) Model spectra calculated from the best-fit cold-coagulation model (model 2; $P = 0.90$, $P' \approx 0.73$, $\alpha \approx 3.1$) with $1 \mu\text{m} < a < 10 \mu\text{m}$ (dotted line), $1 \mu\text{m} < a < 100 \mu\text{m}$ (dashed line), and $1 \mu\text{m} < a < 1 \text{ cm}$ (solid line; same as the solid line in Fig. 1a).

To illustrate the disk regional contribution, we show in Figure 5 the IR emission from dust in the regions of $(r_p - \Delta) < r < r_p$, $r_p < r < (r_p + \Delta)$ and $(r_p - \Delta) < r < (r_p + \Delta)$, as well as $0.15 \text{ AU} < r < 250 \text{ AU}$, calculated from the best-fitting cold-coagulation dust model (model 2; $P = 0.90$, $P' \approx 0.73$, $\alpha \approx 2.9$) with a Gaussian spatial distribution ($r_p = 70 \text{ AU}$, $\Delta = 15 \text{ AU}$). It is seen that the IR emission is exclusively contributed by dust confined in the ring region of $(r_p - \Delta) < r < (r_p + \Delta)$.

So far, all models assume $a_{\min} = 1 \mu\text{m}$. We now consider models with smaller or larger a_{\min} values. In Figure 6a we show the best-fit spectra calculated from models with $a_{\min} = 0.1 \mu\text{m}$ (model 15) and $a_{\min} = 10 \mu\text{m}$ (model 16). It is seen that (1) models with $a_{\min} = 0.1 \mu\text{m}$ emit a bit too much at $\lambda \gtrsim 100 \mu\text{m}$ —decreasing the dust porosity improves the fit at $\lambda \gtrsim 100 \mu\text{m}$, but the fit to the $\lambda \lesssim 10 \mu\text{m}$ part deteriorates—and (2) models with $a_{\min} = 10 \mu\text{m}$ emit too little at $\lambda \lesssim 10 \mu\text{m}$. Increasing the dust porosity does not solve this problem.

To illustrate the IR emission contributed by different dust sizes, we show in Figure 6b the emission spectra calculated from the best-fitting cold-coagulation model (model 2; $P = 0.90$, $P' \approx 0.73$, $\alpha \approx 2.9$) with $1 \mu\text{m} < a < 10 \mu\text{m}$ (these grains are subject to radiative expulsion; see § 3.4), $1 \mu\text{m} < a < 100 \mu\text{m}$ (these grains are subject to P-R inward-spiralling drag; see § 3.4), and $1 \mu\text{m} < a < 1 \text{ cm}$. It is seen that the $\lambda \lesssim 20 \mu\text{m}$ mid-IR emission is dominantly produced by grains smaller than $100 \mu\text{m}$ in radius. Since these grains will be removed from the disk during its lifetime

⁴ This requires that the constituent individual particles should be smaller than the typical interstellar dust ($a \sim 0.1 \mu\text{m}$).

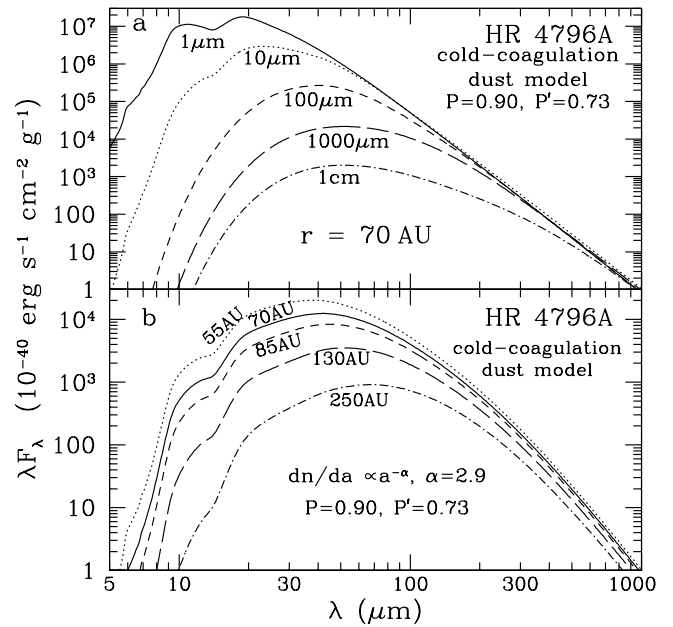


FIG. 7.—(a) IR emission per gram dust mass (received at the Earth) calculated from the $P = 0.90$ ($P' \approx 0.73$) cold-coagulation dust at $r = 70 \text{ AU}$ with a single size of $a = 1 \mu\text{m}$ (solid line), $10 \mu\text{m}$ (dotted line), $100 \mu\text{m}$ (dashed line), $1000 \mu\text{m}$ (long-dashed line), and 1 cm (dot-dashed line). (b) IR emission per gram dust mass calculated from the $P = 0.90$ ($P' \approx 0.73$) cold-coagulation dust at $r = 55 \text{ AU}$ (dotted line), 70 AU (solid line), 85 AU (dashed line), 130 AU (long-dashed line), and 250 AU (dot-dashed line) with a distribution of sizes ($dn/da \propto a^{-\alpha}$, $\alpha = 2.9$, $a \in [1 \mu\text{m}, 1 \text{ cm}]$).

through either radiative expulsion or P-R drag, there must exist a source of replenishment (see § 3.4).

Finally, we show in Figure 7a the IR emission per unit dust mass received at the Earth produced by the $P = 0.90$ ($P' \approx 0.73$) cold-coagulation dust at $r = 70 \text{ AU}$ with a single size of $a = 1, 10, 100$, and $1000 \mu\text{m}$ and 1 cm (at $r = 70 \text{ AU}$, these grains are colder than 110 K and have a porosity of $P' = 0.73$ —their constituent particles are coated by a layer of ice mantles—except the $a = 1 \mu\text{m}$ dust, which attains an equilibrium temperature of $\approx 154 \text{ K}$ and thus has no ice mantles and therefore has a porosity of $P = 0.90$). In Figure 7b we show the IR spectra emitted by a gram of the $P = 0.90$ ($P' \approx 0.73$) cold-coagulation dust at $r = 55, 70, 85, 130$, and 250 AU with a distribution of sizes ($dn/da \propto a^{-\alpha}$, $\alpha = 2.9$, $a \in [1 \mu\text{m}, 1 \text{ cm}]$).

3.3. Is There a “Zodiacal Dust” Component?

In modeling the HR 4796A SED, Koerner et al. (1998) and Augereau et al. (1999) argued that, in addition to the dust responsible for the emission at $\lambda > 20 \mu\text{m}$, a hot “zodiacal dust” component that is confined within ~ 3 – 6 or ~ 9 – 10 AU of the star is required to account for the entire emission at $\lambda \lesssim 12 \mu\text{m}$ and $\lesssim 5\%$ – 10% of the emission at $\lambda \sim 20 \mu\text{m}$. However, it can be seen clearly from Figures 1 and 2 and even the unphysical single-power-law spatial distribution model of Figure 3 that our models closely reproduce the observed SED over the entire wavelength range. There is thus no need to invoke a hot zodiacal dust component; indeed, we may now ask how much such dust can be tolerated based on our models.

An upper limit on the zodiacal dust component can be obtained such that this abundance of hot dust, after being

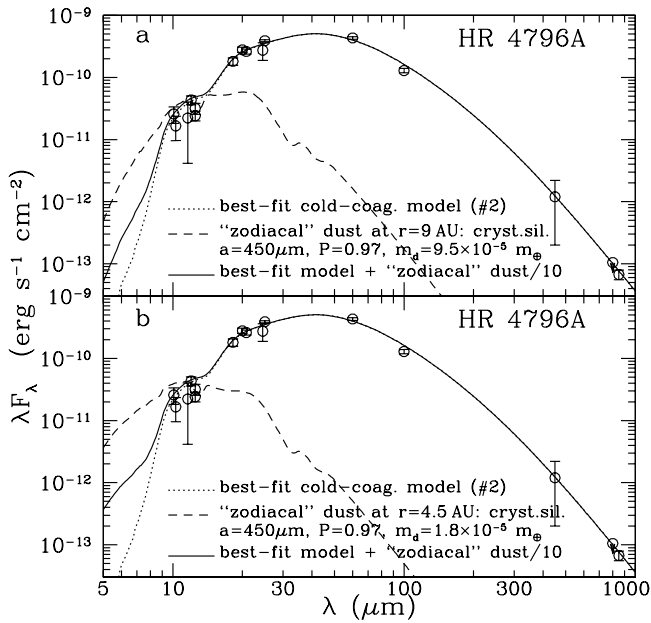


Fig. 8.—Upper limits on the zodiacal dust component at (a) $r = 9$ AU ($m_d \approx 9.5 \times 10^{-6} m_\oplus$) and at (b) $r = 4.5$ AU ($m_d \approx 1.8 \times 10^{-5} m_\oplus$). The dashed lines show the model spectra calculated from the zodiacal dust, which is taken to be porous crystalline silicate dust with $P = 0.97$ and $a = 450 \mu\text{m}$ (see Augereau et al. 1999) of (a) $m_d \approx 9.5 \times 10^{-5} m_\oplus$ at $r = 9$ AU and (b) $m_d \approx 1.8 \times 10^{-5} m_\oplus$ at $r = 4.5$ AU, assuming the emission at $\lambda \lesssim 12 \mu\text{m}$ is entirely produced by the zodiacal dust. The dotted lines show the best-fit cold-coagulation model spectra (model 2; $P = 0.90$, $P' \approx 0.73$, $\alpha \approx 2.9$; same as the solid line in Fig. 1a). The solid lines show the sum of 10% of the zodiacal dust emission and the best-fit cold-coagulation model emission.

added to the IR emission spectra of our best-fitting models (e.g., model 2), would not exceed the observed emission at $\lambda \lesssim 12 \mu\text{m}$. Following Augereau et al. (1999), we assume that the zodiacal dust consists of porous ($P \approx 0.97$) crystalline silicate grains of $a = 450 \mu\text{m}$. As shown in Figure 8, if the observed emission at $\lambda \lesssim 12 \mu\text{m}$ is entirely produced by the zodiacal dust, a total amount of $m_d \approx 9.5(1.8) \times 10^{-5} m_\oplus$ is required if the zodiacal dust lies at $r = 9(4.5)$ AU. It is seen in Figure 8 that our best-fitting model (model 2) allows at most 10% of this mass to be in the zodiacal dust component.

The reason why Koerner et al. (1998) required a population of zodiacal dust can be ascribed to the fact that they have not considered a distribution of dust sizes; instead, they simply approximated the dust emissivity ϵ_λ as a one-parameter function: $\epsilon_\lambda = 1$ for $\lambda < a_0$ and $\epsilon_\lambda = a_0/\lambda$ for $\lambda > a_0$, where a_0 is a parameter characteristics of dust size. It would not be surprising if their model lacks hot dust emitting at $\lambda \lesssim 12 \mu\text{m}$ since their approximation is essentially for single-sized dust models.

The reason why Augereau et al. (1999) needed a population of zodiacal dust may lie in the fact that they fixed the power index of their dust size distribution to be $\alpha = 3.5$. Using a steeper size distribution (in comparison with $\alpha = 2.8\text{--}2.9$ of our $P = 0.90$ best-fitting models 2 and 6; see Figs. 1 and 2), Augereau et al. (1999) had to raise a_{min} to $\gtrsim 10 \mu\text{m}$ in order to reproduce the long-wavelength emission. This led to a paucity of small grains that are hot enough to emit at $\lambda \lesssim 12 \mu\text{m}$ (this can also be seen from the dotted line in Fig. 6a).

Also arguing against attributing the $\lambda \lesssim 12 \mu\text{m}$ emission to a hot zodiacal dust component are the recent 10.8 and

18.2 μm mid-IR images of the HR 4796A disk that show that the disk's size at 10 μm is comparable to its size at 18 μm (Telesco et al. 2000). This implies that the 18 μm -emitting dust may also emit some, or all, of the 10 μm radiation (Telesco et al. 2000). This is in sharp contrast to the zodiacal dust assumption, which suggested that the zodiacal dust component contributes only $\lesssim 5\%\text{--}10\%$ of the 20 μm emission (Koerner et al. 1998; Augereau et al. 1999).

The tidal effects produced by sweeping inner planets together with the P-R drag may be responsible for the absence of a warm zodiacal dust population as well as the presence of an inner-disk hole ($r \lesssim 50$ AU).

3.4. Radiation Pressure and Poynting-Robertson Drag

In addition to the gravitational attraction from the central star, grains in the HR 4796A disk are subject to (1) radiative repulsion due to the momentum carried by stellar photons and (2) P-R drag, which takes both energy and momentum from their orbits and causes them to spiral toward the gravitational force center (Burns, Lamy, & Soter 1979; Backman & Paresce 1993).

We have calculated β_{RP} —the ratio of radiative pressure (RP) force to gravitational force for the best-fitting cold-coagulation dust (model 2; $P = 0.90$, $P' \approx 0.73$) and hot-nebula dust (model 6; $P = 0.90$, $P' \approx 0.80$). As shown in Figure 9a, for grains smaller than $\sim 10\text{--}20 \mu\text{m}$, the radiation pressure overcomes the gravitational attraction (i.e., $\beta_{\text{RP}} \gtrsim 1$), and therefore, these grains will be blown out from the HR 4796A disk. The dust removal rate due to the

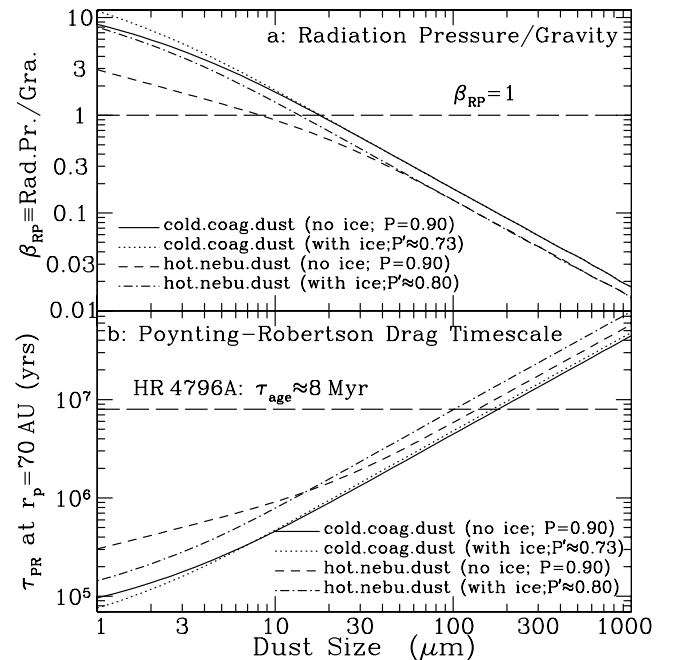


Fig. 9.—(a) Ratios of the radiative repulsion to the gravitational attraction (β_{RP}) for the best-fitting cold-coagulation dust (without ice $P = 0.90$ [solid line] or with ice $P' = 0.73$ [dotted line]) and the hot-nebula dust (without ice $P = 0.90$ [dashed line] or with ice $P' = 0.80$ [dot-dashed line]). The long-dashed horizontal line plots $\beta_{\text{RP}} = 1$. (b) Orbit decay timescales $\tau_{\text{P-R}}$ due to the P-R drag for the best-fitting cold-coagulation dust (without ice $P = 0.90$ [solid line] or with ice $P' = 0.73$ [dotted line]) and the hot-nebula dust (without ice $P = 0.90$ [dashed line] or with ice $P' = 0.80$ [dot-dashed line]) at a radial distance of $r = 70$ AU from the central star (note $\tau_{\text{P-R}} \propto r^2$). The long-dashed horizontal line plots the HR 4796A age (≈ 8 Myr).

TABLE 2
DUST IR EMISSION AVERAGED OVER *SIRTF* BANDS PREDICTED FOR OUR PREFERRED MODELS

Model	IRAC 3.6 μm (Jy)	IRAC 4.5 μm (Jy)	IRAC 5.8 μm (Jy)	IRAC 8.0 μm (Jy)	MIPS 24 μm (Jy)	MIPS 70 μm (Jy)	MIPS 160 μm (Jy)
2.....	1.18×10^{-8}	9.81×10^{-7}	5.09×10^{-5}	7.39×10^{-3}	2.63	7.26	2.94
6.....	3.44×10^{-9}	3.91×10^{-7}	2.18×10^{-5}	1.67×10^{-3}	2.85	6.61	2.58
13.....	1.31×10^{-8}	9.51×10^{-7}	4.62×10^{-5}	6.62×10^{-3}	2.56	7.81	3.41
14.....	3.68×10^{-9}	3.74×10^{-7}	1.98×10^{-5}	1.51×10^{-3}	2.79	7.12	2.99

radiation pressure expulsion can be estimated by integrating $(4\pi/3)\rho a^3/\tau_{\text{RP}}(r)$ over the size range $1 \mu\text{m} < a < 10 \mu\text{m}$ and over the entire disk. Assuming that the RP timescale is comparable to the local dynamical timescale [$\tau_{\text{RP}}(r) \approx 370(r/70 \text{ AU})^{3/2} \text{ yr}$], we estimate the RP dust mass-loss rate to be $\approx 8.19 \times 10^{-7} m_{\oplus} \text{ yr}^{-1}$ for the best-fitting cold coagulation model (model 2) and $\approx 8.28 \times 10^{-7} m_{\oplus} \text{ yr}^{-1}$ for the best-fitting hot-nebula model (model 6).

We have also calculated the P-R drag timescales ($\tau_{\text{P-R}}$). In Figure 9b we show that, for grains smaller than $\sim 100\text{--}200 \mu\text{m}$ at a radial distance of $r = 70 \text{ AU}$ from the central star, their lifetimes (at $r = 70 \text{ AU}$) due to the P-R drag effect are shorter than the HR 4796A age, and hence, grains in the range of $10\text{--}20 \mu\text{m} \lesssim a \lesssim 100\text{--}200 \mu\text{m}$, although stable against radiation pressure ejection, could be removed from the disk by the P-R drag. Since the best-fitting models have $\lesssim 30\%\text{--}40\%$ of the total surface areas in grains smaller than $100 \mu\text{m}$, these grains must be efficiently replenished by cascade collisions of planetesimals and larger grains which are responsible for the mid-IR emission at $\lambda \lesssim 20 \mu\text{m}$ (see Fig. 6b), otherwise there would be little mid-IR emission at $\lambda \lesssim 20 \mu\text{m}$. By integrating the P-R dust removal rate $(4\pi/3)\rho a^3/\tau_{\text{P-R}}(a, r)$ over the whole size range and over the entire disk, we estimate the P-R dust mass-loss rate to be $\approx 9.22 \times 10^{-9} m_{\oplus} \text{ yr}^{-1}$ for the best-fitting cold-coagulation model (model 2) and $\approx 7.96 \times 10^{-9} m_{\oplus} \text{ yr}^{-1}$ for the best-fitting hot-nebula model (model 6).

Therefore, over the life span of HR 4796A, roughly $6.7 m_{\oplus}$ of dust is lost by radiation pressure and P-R drag, which is about 3 times smaller than the estimation of Augereau et al. (1999; $\approx 20 m_{\oplus}$). This is mainly because Augereau et al. (1999) attributed the dominant dust removal process to grain-grain collisions. We consider this unlikely since grain-grain collisions would not remove the dust from the disk; instead, they just redistribute the dust over different size bins through fragmentation or sticking.⁵

It is well established (see, e.g., Spangler et al. 2001; Zuckerman & Becklin 1993) that the amount of IR excess around MS stars decreases with the star's age. There are at least two possible explanations for this result: (1) the particles are lost by the P-R drag effect and (2) the particles have coalesced into larger bodies that are undetectable as the opacity per gram decreases ($\kappa_{\text{abs}} \propto 1/a$; see § 3). For the HR 4796A disk, the latter process seems to be the dominant one, as reflected by its collisionally replenished *secondary* nature—the amount of dust incorporated into larger bodies that acts

⁵ Since the grain-grain collision timescale $\tau_{\text{coll}} \approx 2\pi[(a^2)\sigma(r)\Omega(r)]^{-1} \approx 670 \text{ yr}$ at $r = 70 \text{ AU}$ [$\Omega(r) \equiv (GM_*/r^3)^{1/2}$ is the Keplerian frequency; M_* ($\approx 2.5 m_{\odot}$) is the stellar mass; G is the gravitation constant] is comparable to the RP timescale $\tau_{\text{RP}} \approx 370 \text{ yr}$ (at $r = 70 \text{ AU}$), a stable population of $a < 10 \mu\text{m}$ dust can also be obtained through a cascade production during collisions between larger grains.

as a source of replenishment must be much larger than that of the dust lost through P-R drag.

3.5. Predictions for *SIRTF*

SIRTF will be capable of sensitive imaging using the IRAC at 3.6, 4.5, 5.8, and 8.0 μm and using the MIPS at 24, 70, and 160 μm . In Table 2 we show the band-averaged intensities for our preferred dust models.

SIRTF will also be able to perform low-resolution 5–40 μm and high-resolution 10–37 μm spectroscopic observations using the Infrared Spectrograph instrument. IR spectroscopy and imaging will provide powerful constraints on the HR 4796A dust spatial distribution and its chemical composition. The cold-coagulation dust models all predict an almost featureless SED (the 9.7 μm amorphous silicate feature is very broad and smooth).⁶ In contrast, the hot-nebula dust models predict two sharp crystalline silicate features at 11.3 and 23 μm . In order to produce noticeable 11.3 and 23 μm features, at least 20% of the silicate dust must be in the crystalline form. *SIRTF* spectroscopy will allow us to infer the degree of processing that the HR 4796A dust has experienced.

4. CONCLUSION

We have modelled the mid-infrared-to-submillimeter SED of the ringlike dust disk around the dustiest $\sim 8 \text{ Myr}$ old A-type star HR 4796A. We start with two extreme dust types: one formed through cold coagulation of unaltered protostellar interstellar grains and one formed through aggregation of grains highly processed in the protostellar nebula with silicate dust annealed and carbon dust oxidized. We adopt a Gaussian-type dust spatial distribution with a peak at 70 AU from the central star and an FWHM of 15 AU as inferred from images of scattered light and dust thermal emission. We take a simple power law for the dust size distribution ($dn/da \propto a^{-\alpha}$, with $\alpha \approx 2.8\text{--}2.9$) in the range of $1 \mu\text{m} \lesssim a \lesssim 1 \text{ cm}$. Our principal results are as follows:

1. It is shown that both types of dust are successful in reproducing the observed SED, provided that the dust gen-

⁶ The 3.3, 6.2, 7.7, 8.6, and 11.3 μm vibrational bands characteristic for polycyclic aromatic hydrocarbon (PAH) molecules are not seen in our model spectra, although their presence in the HR 4796A disk is expected in the context of the cold-coagulation model since PAHs are a significant constituent of interstellar dust (see, e.g., Li & Draine 2001b). This is mainly because PAHs have condensed in the icy mantles of the porous aggregates at $r \gtrsim 70 \text{ AU}$ and those icy aggregates are too cold to evaporate their ice mantles so as to eject PAHs (see § 4 in Li & Lunine 2003). In the inner regions of the disk, PAHs, sublimated from the icy mantles, would be rapidly photodissociated. Therefore, PAHs are not considered in this paper. The presence of PAHs in dusty disks will be discussed in a subsequent paper.

erated by collisions of planetesimals and cometesimals is highly fluffy, with a vacuum volume fraction of $\sim 90\%$ (§ 2). The fact that the dust in the HR 4796A disk must be somewhere intermediate between these two types implies that our models are robust. Future high-resolution spectroscopy of the HR 4796A disk would allow us to infer the degree to which the dust has been processed (§ 3.1).

2. Although models with a single-power-law spatial distribution are also able to reproduce the observed SED, the derived dust distribution is both unphysical and inconsistent with the imaging observations of scattered light and dust mid-IR thermal emission (§ 3.2).

3. Our models show no evidence for the existence of a hot zodiacal dust component suggested to lie at a radial distance of a few astronomical units from the star by previous workers to account for the emission at $\lambda \lesssim 12 \mu\text{m}$ (§ 3.3). Our upper limit on the total mass of this component is at least 10

times smaller than what would be obtained if the entire $\lambda \lesssim 12 \mu\text{m}$ emission is attributed to this hot dust.

4. Grains smaller than $\sim 10\text{--}20 \mu\text{m}$ will be radiatively expelled from the disk; grains at $r = 70 \text{ AU}$ in the range of $\sim 10\text{--}20 \mu\text{m} \lesssim a \lesssim 100\text{--}200 \mu\text{m}$ will also be removed from the disk because of the P-R inward-spiraling drag (*closer* to the star, *larger* grains will be removed). Collisions of planetesimals/cometesimals must continuously replenish the dust in the disk at a rate of $\approx 8.3 \times 10^{-7} m_{\oplus} \text{ yr}^{-1}$ (§ 3.4).

We thank A. G. W. Cameron, S. E. Strom, and the anonymous referee for helpful comments and suggestions. A. Li thanks the University of Arizona for the Arizona Prize Postdoctoral Fellowship in Theoretical Astrophysics. This research was supported in part by grants from the NASA origins research and analysis program.

APPENDIX A

POSSIBLE DUST COMPOSITION FOR COLD PROTOPLANETARY DISK

The coagulation of interstellar grains that results in fluffy and inhomogeneous aggregates occurs in cold, dense, molecular clouds and protostellar and protoplanetary dust disks. It plays an important role in the formation of planetary systems (Weidenschilling & Cuzzi 1993). In this section we approximately derive the proportional composition of the dust in circumstellar disks around (pre-) MS stars from the abundances of the condensable elements (C, N, O, Si, Fe, and Mg),⁷ assuming that protostellar activities impose little modification on protostellar grain compositions (see Beckwith et al. 2000).

Let $[X/H]_{\odot}$ be the cosmic abundance of X relative to H (we assume that the cosmic elemental abundances are those of the solar values: $[C/H]_{\odot} \approx 391$ parts per million (ppm), $[N/H]_{\odot} \approx 85.2$ ppm, $[O/H]_{\odot} \approx 545$ ppm, $[Mg/H]_{\odot} \approx 34.5$ ppm, $[Fe/H]_{\odot} \approx 34.4$ ppm, and $[Si/H]_{\odot} \approx 28.1$ ppm; Sofia & Meyer 2001); let $[X/H]_{\text{gas}}$ be the amount of X in gas phase ($[C/H]_{\text{gas}} \approx 140$ ppm, $[N/H]_{\text{gas}} \approx 61$ ppm, $[O/H]_{\text{gas}} \approx 310$ ppm; Fe, Mg, and Si are highly depleted in dust; see Li & Greenberg 1997 and references therein); let $[X/H]_{\text{dust}}$ be the amount of X relative to H locked up in dust ($[C/H]_{\text{dust}} = [C/H]_{\odot} - [C/H]_{\text{gas}} \approx 251$ ppm, $[N/H]_{\text{dust}} \approx 24.2$ ppm, $[O/H]_{\text{dust}} \approx 235$ ppm, $[Mg/H]_{\text{dust}} \approx 34.5$ ppm, $[Fe/H]_{\text{dust}} \approx 34.4$ ppm, $[Si/H]_{\text{dust}} \approx 28.1$ ppm). Assuming a stoichiometric composition of MgFeSiO_4 for interstellar silicates, the total mass of silicate dust per H atom is $m_{\text{sil}} \approx [Fe/H]_{\text{dust}} \mu_{\text{Fe}} + [Mg/H]_{\text{dust}} \mu_{\text{Mg}} + [Si/H]_{\text{dust}} \mu_{\text{Si}} + [O/H]_{\text{sil}} \mu_{\text{O}} \approx 5.61 \times 10^{-3} \mu_{\text{H}}$, where μ_{X} is the atomic weight of X in units of $\mu_{\text{H}} \approx 1.66 \times 10^{-24} \text{ g}$ and $[O/H]_{\text{sil}} \approx 4\{[Fe/H]_{\text{dust}} + [Mg/H]_{\text{dust}} + [Si/H]_{\text{dust}}\}/3 \approx 129$ ppm is the amount of O in silicate dust per H atom (i.e., we assign four O atoms for the average of the Fe, Mg, and Si abundances). The carbonaceous dust component is dominated by C, with little H, N, and O (we assume $H/C = 0.5$, $O/C = 0.1$). The total mass of carbon dust per H atom is $m_{\text{carb}} \approx [C/H]_{\text{dust}} \mu_{\text{C}} + [N/H]_{\text{dust}} \mu_{\text{N}} + 0.5[C/H]_{\text{dust}} \mu_{\text{H}} + 0.1[C/H]_{\text{dust}} \mu_{\text{O}} \approx 3.88 \times 10^{-3} \mu_{\text{H}}$. The C, O, and N atoms left over after accounting for the silicate and carbon dust components are assumed to condense in icy grains in the form of H_2O , NH_3 , CO , CO_2 , CH_3OH , and CH_4 (following Greenberg 1998, we assume $\text{CO} : \text{CO}_2 : \text{CH}_3\text{OH} : \text{CH}_4 : \text{H}_2\text{CO} = 10 : 4 : 3 : 1 : 1$). The total mass of icy grains per H atom is $m_{\text{ice}} \approx m_{\text{ice}}^{\text{C}} + m_{\text{ice}}^{\text{N}} + m_{\text{ice}}^{\text{water}}$, where the mass of C-containing ice $m_{\text{ice}}^{\text{C}} \approx [C/H]_{\text{gas}} \mu_{\text{C}} + [C/H]_{\text{gas}} (22\mu_{\text{O}} + 18\mu_{\text{H}})/19 \approx 2.87 \times 10^{-3} \mu_{\text{H}}$; the mass of NH_3 ice $m_{\text{ice}}^{\text{N}} \approx [N/H]_{\text{gas}} (\mu_{\text{N}} + 3\mu_{\text{H}}) \approx 4.10 \times 10^{-4} \mu_{\text{H}}$; the mass of water ice $m_{\text{ice}}^{\text{water}} \approx [O/H]_{\text{water}} (\mu_{\text{O}} + 2\mu_{\text{H}}) \approx 4.12 \times 10^{-3} \mu_{\text{H}}$; and $[O/H]_{\text{water}} \approx [O/H]_{\odot} - [O/H]_{\text{sil}} - 0.1[C/H]_{\text{dust}} - 22[C/H]_{\text{gas}}/19 \approx 229$ ppm is the amount of O locked up in H_2O ice (we assume H_2O contains all the remaining available O).

Therefore, as a first approximation, we may assume a mixing ratio of $m_{\text{carb}}/m_{\text{sil}} \approx 0.7$ and $m_{\text{ice}}/(m_{\text{sil}} + m_{\text{carb}}) \approx 0.8$ for cold regions (for hot regions where ices sublimate, the dust can be simply modeled as porous aggregates of silicate and carbon particles with $m_{\text{carb}}/m_{\text{sil}} \approx 0.7$). This does not deviate much from the in situ measurements of cometary dust ($m_{\text{carb}}/m_{\text{sil}} \approx 0.5$, $m_{\text{ice}}/[m_{\text{sil}} + m_{\text{carb}}] \approx 1.0$; see Greenberg & Li 1999 and references therein), which is often suggested to be a porous aggregate of unaltered interstellar dust (Greenberg 1998; Greenberg & Li 1999).

APPENDIX B

DUST MORPHOLOGY

Dust formed through coagulation of many small subgrains has a porous structure. Let v_{sil} and v_{carb} be the total volumes taken up by the silicate and carbonaceous dust components, respectively, P be the porosity—the fractional volume of vacuum—and $\rho_{\text{sil}} (\approx 3.5 \text{ g cm}^{-3})$ and $\rho_{\text{carb}} (\approx 1.8 \text{ g cm}^{-3})$ be the mass densities of silicate and carbonaceous materials, respectively. The mass density for a fluffy aggregate of silicate and carbonaceous subgrains with a porosity of P is $\langle \rho \rangle = (1 - P)(\rho_{\text{sil}} v_{\text{sil}} + \rho_{\text{carb}} v_{\text{carb}})/(v_{\text{sil}} + v_{\text{carb}})$. In regions colder than $\approx 110\text{--}120 \text{ K}$, preexisting or recondensed ices around the silicate and

⁷ Some H will be present, mostly in combination with O, C, and N.

carbonaceous dust cores would fill all or part of the vacuum in the aggregate. Let v_{ice} be the total volume taken up by the ice component and ρ_{ice} ($\approx 1.2 \text{ g cm}^{-3}$) be the ice mass density. The porosity for the fluffy aggregate of ice-coated silicate and carbonaceous subgrains would be reduced to $P' = \max\{0, 1 - (1 - P)[1 + v_{\text{ice}}/(v_{\text{sil}} + v_{\text{carb}})]\}$. Its mean mass density is $\langle \rho' \rangle = (1 - P')(\rho_{\text{sil}}v_{\text{sil}} + \rho_{\text{carb}}v_{\text{carb}} + \rho_{\text{ice}}v_{\text{ice}})/(v_{\text{sil}} + v_{\text{carb}} + v_{\text{ice}})$. The dust “size” is defined as the radius of the sphere that encapsulates the whole fluffy aggregate. The mean mass densities defined here are independent of aggregate size.

REFERENCES

- Augereau, J. C., Lagrange, A. M., Mouillet, D., Papaloizou, J. C. B., & Gorod, P. A. 1999, *A&A*, 348, 557
- Backman, D. E., & Paresce, F. 1993, in *Protostars and Planets III*, ed. E. H. Levy & J. I. Lunine (Tucson: Univ. Arizona Press), 1253
- Beckwith, S. V. W., Henning, Th., & Nakagawa, Y. 2000, in *Protostars and Planets IV*, ed. V. Mannings, A. P. Boss, & S. S. Russell (Tucson: Univ. Arizona Press), 533
- Bohren, C. F., & Huffman, D. R. 1983, *Absorption and Scattering of Light by Small Particles* (New York: Wiley)
- Burns, J. A., Lamy, P. L., & Soter, S. 1979, *Icarus*, 40, 1
- Cameron, A. G. W., & Schneck, P. B. 1965, *Icarus*, 4, 396
- Draine, B. T., & Lee, H. M. 1984, *ApJ*, 285, 89
- Gail, H.-P. 2001, *A&A*, 378, 192
- Greenberg, J. M. 1998, *A&A*, 330, 375
- Greenberg, J. M., & Li, A. 1999, *Space Sci. Rev.*, 90, 149
- Jayawardhana, R., Fisher, R. S., Hartmann, L., Telesco, C. M., Piña, R. K., & Fazio, G. 1998, *ApJ*, 503, L79
- Jura, M. 1991, *ApJ*, 383, L79
- Jura, M., Ghez, A. M., White, R. J., McCarthy, D. W., Smith, R. C., & Martin, P. G. 1995, *ApJ*, 445, 451
- Jura, M., Malkan, M., White, R., Telesco, C. M., Piña, R. K., & Fisher, R. S. 1998, *ApJ*, 505, 897
- Jura, M., Zuckerman, B., Becklin, E. E., & Smith, R. C. 1993, *ApJ*, 418, L37
- Kenyon, S. J., Wood, K., Whitney, B. A., & Wolff, M. J. 1999, *ApJ*, 524, L119
- Klahr, H. H., & Lin, D. N. C. 2001, *ApJ*, 554, 1095
- Koerner, D. W., Ressler, M. E., Werner, M. W., & Backman, D. E. 1998, *ApJ*, 503, L83
- Kurucz, R. L. 1979, *ApJS*, 40, 1
- Li, A., & Draine, B. T. 2001a, *ApJ*, 550, L213
- . 2001b, *ApJ*, 554, 778
- Li, A., & Greenberg, J. M. 1997, *A&A*, 323, 566
- . 1998, *A&A*, 331, 291
- Li, A., & Lunine, J. I. 2003, *ApJ*, submitted
- Schneider, G., et al. 1999, *ApJ*, 513, L127
- Shu, F. H., Shang, H., & Lee, T. 1996, *Science*, 271, 1545
- Sitko, M. L., Lynch, D. K., & Russell, R. W. 2000, *AJ*, 120, 2609
- Sofia, U. J., & Meyer, D. M. 2001, *ApJ*, 554, L221
- Spangler, C., Sargent, A. I., Silverstone, M. D., Becklin, E. E., & Zuckerman, B. 2001, *ApJ*, 555, 932
- Telesco, C. M., et al. 2000, *ApJ*, 530, 329
- Weidenschilling, S. J., & Cuzzi, J. N. 1993, in *Protostars and Planets III*, ed. E. H. Levy & J. I. Lunine (Tucson: Univ. Arizona Press), 1031
- Wooden, D. H. 2002, *Earth Moon Planets*, 89, 247
- Wyatt, M. C., Dermott, S. F., Telesco, C. M., Fisher, R. S., Grogan, K., Holmes, E. K., & Piña, R. K. 1999, *ApJ*, 527, 918
- Zuckerman, B., & Becklin, E. E. 1993, *ApJ*, 414, 793